1

ION–SURFACE INTERACTIONS

Uwe Thumm

Department of Physics, Kansas State University,
Manhattan, KS 66506, USA

For **low charge states** *of the incident ion, quantum mechanical close–coupling calculations for a single active electron provide detailed information on resonance formation, hybridization, and electron transfer. In contrast, for collisions of slow* **highly charged** *ions with surfaces, ab–initio quantum mechanical calculations cannot be performed, due to the many–electron nature of the inherent formation and decay of multiply excited projectiles. In this paper, some aspects of ion–surface collisions are discussed within quantum mechanical wave function expansion and propagation techniques and within an extended classical over–barrier model.*

1. Introduction

During the past decade, detailed quantum mechanical calculations have become available for interactions of hydrogenic projectiles of low charge with surfaces [1–8]. These calculations are limited to a single active electron whose interaction with the many–particle system given by the moving projectile and a surface is represented by an effective potential. They provide level shifts, transition rates, and hybridization characteristics. Trends and scaling laws in these results provide valuable insight into electron exchange and emission mechanisms and may be used as input and guidelines for more complex collision scenarios, e.g., interactions with highly charged projectile ions (HCI).

The detailed theoretical description of collisions between HCIs and surfaces constitutes a major challenge due to a multitude of possible interactions that are non–perturbative near the surface and involve many active electrons or quasi particles (plasmons, excitons, and phonons). In such encounters, an HCI, say Bi^{46+}, may capture more than 20 electrons into excited states, leading to the formation of a multiply excited, highly unstable, "hollow" ion on the projectile's incident trajectory within a collision time of the order of ten femtoseconds. The modeling of the physics involved in the formation and decay of hollow projectiles is still mostly based on intuition and estimated transition rates, rather than on a detailed quantum dynamical theory. Nevertheless, during the past ten years significant progress has been made, both in understanding the electron capture sequence at large distances from the surface within classical over–barrier models (COM) [9] and, more recently, in extending these models to obtain a more comprehensive, though still incomplete, picture of the mechanisms governing multiple capture, loss, and emission of electrons of an HCI near and inside a solid surface [10–15].

This paper covers some complementary elements of recent theoretical approaches to ion–surface interactions. In Section 2, *ab–initio* quantum mechanical models that are

2

appropriate for collisions with hydrogenic and bare ions of low nuclear charge are discussed. Section 3 reviews the COM with extensions that account for near–surface interactions, appropriate for incident HCIs. Unless stated otherwise, atomic units are used.

2. *Ab–initio* models

2.1. *Close–coupling expansions*

2.1.1. *The self–energy method*

This method [6,9] consists of two major steps. First, a set of resonance basis states

$$|\Phi_i(D)\rangle = \sum_j a_j(t)\,\psi_j(\vec{r})\,e^{-i\epsilon_j t}\; + \;\int d\vec{k}\,\rho(\vec{k})\,b_{\vec{k}}(t)\,\phi_{\vec{k}}(\vec{r})\,e^{-i\epsilon_{\vec{k}} t} \tag{1}$$

is computed as approximate solutions to the time–dependent Schrödinger equation,

$$i|\dot{\Psi}(t)\rangle = H|\Psi(t)\rangle\;,\quad H = T + V_{\mathrm{s}} + V_{\mathrm{c}}^{>}(t) + Fz = H_i + V_i = H_f + V_f\;, \tag{2}$$

for a set of *fixed* projectile–surface distances D, i.e., by neglecting the motion of the projectile. The adiabatic basis states $\Phi_i(D)$ are obtained i.) by using the two–center expansion (1) of $\Phi_i(D)$ in terms of bound atomic states ψ_j of energy ϵ_j and metal surface states $\phi_{\vec{k}}$ of energy $\epsilon_{\vec{k}}$ and ii.) by formally eliminating the expansion coefficients $b_{\vec{k}}$ at the expense of introducing a complex optical potential, also referred to as *self–energy*. This self–energy has a simple pole E that can be determined iteratively, but is commonly replaced by a suitable average over asymptotic atomic energies ϵ_j. The "dressed" projectile states $\Phi_i(D)$ are obtained as eigenfunctions of the complex non-hermitian self–energy matrix with complex eigenvalues $\Omega_i = E_i - i\,\Gamma_i/2$ and are given as linear combinations of the bound atomic basis orbitals.

T designates is the kinetic energy in (2). In the surface potential

$$V_{\mathrm{s}}(z) = \begin{cases} -V_0 & ;\quad z < z_0 \\ V_{\mathrm{e}}^{(\mathrm{i})}(z) + V_{\mathrm{c}}^{(\mathrm{i})}(z;D) & ;\quad z \geq z_0 \end{cases} \tag{3}$$

the z–axis is perpendicular to the metal surface and z_0 is determined by matching $V_{\mathrm{e}}^{(\mathrm{i})}(z_0) + V_{\mathrm{c}}^{(\mathrm{i})}(z_0;D)$ and $-V_0$. The electronic self–image potential and the image potential induced by the projectile–core Coulomb potential (screened inside the metal), $V_{\mathrm{c}}^{>}(t)$, are given by

$$V_{\mathrm{e}}^{(\mathrm{i})}(z) = -\frac{1}{4z}\,\Theta(z) \quad \text{and} \quad V_{\mathrm{c}}^{(\mathrm{i})}(\vec{r};D) = \frac{Z}{|\vec{r} + D\hat{e}_z|}\,\Theta(z) \approx \frac{Z}{|z + D|}\,\Theta(z). \tag{4}$$

The metal basis states $\phi_{\vec{k}}$ are chosen as eigenstates to the initial channel Hamiltonian $H_i = T - V_0\Theta(-z)$. The atomic orbitals ψ_j are eigenfunctions to the atomic Coulomb Hamiltonian $H_f = T + V_C$. $V_{i,f} = H - H_{i,f}$ defines the channel perturbation potentials.

Fig. 1 shows adiabatic resonance energies E_i, calculated as real parts of the eigenvalues Ω_i of the self–energy matrix at fixed distances D and for the magnetic quantum number $m = 0$. Noteworthy is a sequence of narrowly avoided crossings. For example, the adiabatic curves labeled as "5σ" and "6σ" cross and merge asymptotically into the n=3 manifold of
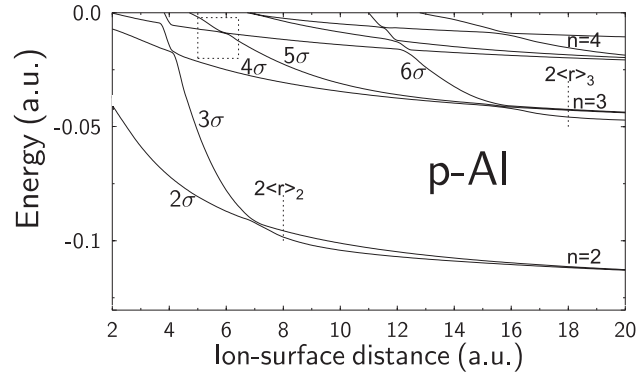
Fig. 1   Adiabatic resonance energies E_i for protons near an aluminum surface

hydrogen. Contour plots of the probability densities of the corresponding wave functions $\Phi_i(D)$ inside (at $D = 5$) and outside (at $D = 6$) the avoided crossing at $D \approx 5.8$ in Fig. 2 show that the characteristics of the resonance wave function (i.e., the wave function's nodal structure and widths) are carried *diabatically* through the crossing. This suggests the use of *diabatized* adiabatic resonance states $\tilde{\Phi}_i(D)$ of complex energies $\tilde{\Omega}_i = \tilde{E}_i - i\tilde{\Gamma}_i/2$ that are identical to (relabeled) adiabatic states $\Phi_i(D)$, except at energies very close to curve crossings.
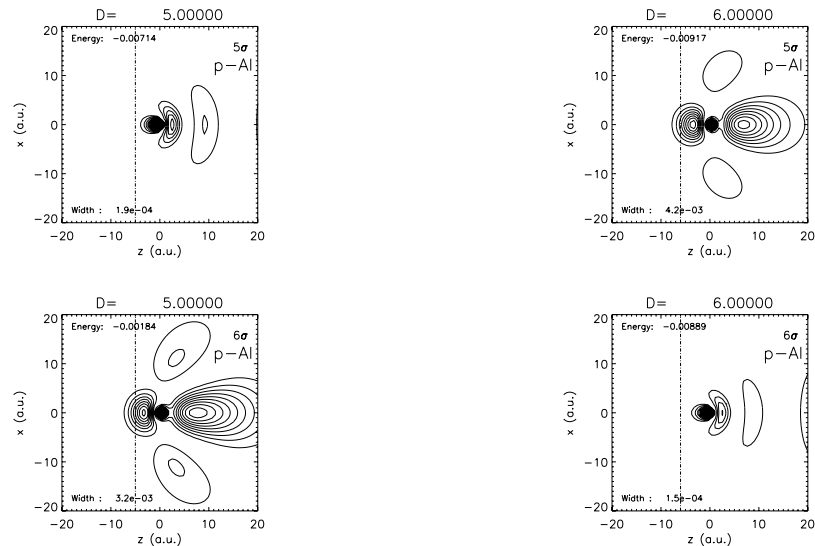

Fig. 2   Probability densities of adiabatic resonance states "5σ" and "6σ" near the avoided crossing at $D \approx 5.8$ in Fig. 1

In the second step, dynamical couplings induced by a *moving* projectile are included by expanding the solution $\Psi(t)$ of the time-dependent one-electron Schrödinger equation (2)

4

in terms of the resonance states $\tilde{\Phi}_i(D(t))$,

$$|\Psi(\vec{r};t)> = \sum_{i=1}^{N} c_i(t)\ |\tilde{\Phi}_i(\vec{r};D(t)) > \ \exp[-i\int^t dt'\tilde{E}_i(D(t'))]\ . \qquad (5)$$

Inserting this expansion into equation (1) leads to the set of close–coupling equations

$$\dot{c}_i(t) = -\sum_{i'=1}^{N}\ c_{i'}(t)\ \langle\tilde{\Phi}_i|\frac{\partial}{\partial t} + \frac{\tilde{\Gamma}_i}{2}\delta_{ii'}|\tilde{\Phi}_{j'}\rangle \exp[-i\int^t dt'(\tilde{E}_{i'} - \tilde{E}_i)]\ . \qquad (6)$$

The operator $\partial/\partial t \equiv -v_z\partial/\partial D$ gives rise to velocity-dependent off-diagonal ("dynamic") couplings between the resonance states $\tilde{\Phi}_i$. The diagonal width term $\tilde{\Gamma}_i/2$ describes the decay, induced by the potential couplings between the atom and metal sub–spaces, of resonance states $\tilde{\Phi}_i$ with energy above the Fermi level of the metal into empty metal states. By suppressing the dynamic couplings in Eqs. (6), we retrieve classical rate equations [7] .

In order to approach the conditions of current experiments [16], we included the effect of a uniform electric field F along the surface normal on the ionization probability P_{ion} [7]. The incident hydrogen atoms are assumed to be prepared in the statistically populated $n = 5, m = 0$ manifold. Fig. 3 shows the ionization probability at the time the atom has approached an Al surface to a distance D, both with (solid lines) and without (dashed lines) dynamic couplings in Eq. (6).   The external electric field has a very small effect
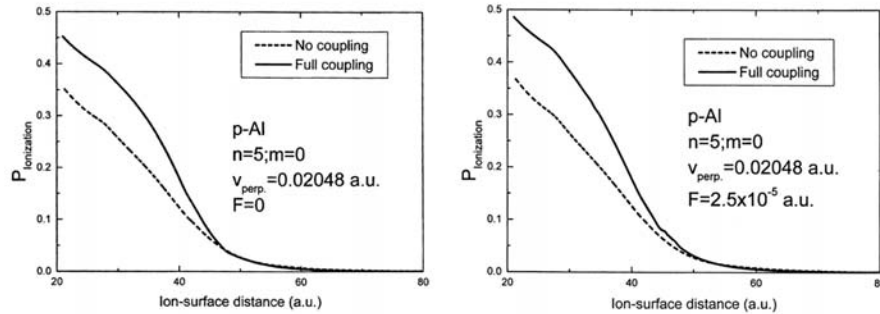

Fig. 3   Ion production probability for excited hydrogen atoms perpendicularly incident on an aluminum surface at speed $v_z = 2 \times 10^{-2}$. Left: without; right: with an external field of strength $F = 2.5 \times 10^{-5}$.

for distances $D > 40$. When the velocity is raised from $v_z = 2 \times 10^{-5}$ to 2×10^{-2}, ion production sets in at shorter distances and tends to be smaller throughout, as expected in view of the shorter time available for the decay of the resonance states. The effect of the dynamic couplings is very small at $v_z = 2 \times 10^{-5}$ and a classical rate–equation approach is justified for sub–thermal velocities. As shown in the Fig., at $v_z = 2 \times 10^{-2}$, however, dynamic couplings influence the ion production significantly, and demand a fully time–dependent, quantum mechanical treatment.

2.1.2. The continuum–discretization method

In the self–energy approach, different metal states can interact only indirectly, via projectile states. Off–diagonal couplings within the metal sub–space are taken into account in an alternative method, by discretizing the continuum of conduction band states and by replacing this continuum with a finite number of wave packets ("Weyl packets"),

$$\phi_n(z) = \sqrt{\frac{\delta_z}{2\pi}} \left\{ \frac{2\sin(\delta_z z/2)}{\delta_z z} \left[e^{ik_n z} + R_n e^{-ik_n z} \right] \theta(-z) + T_n e^{-\gamma_n z} \theta(z) \right\} . \qquad (7)$$

Each wave packet (7) is obtained by superimposing eigenfunctions to a potential step of height V_0 at the surface within a narrow interval of electron momenta along the surface normal. These intervals have a width δ_z and centroid momenta k_n, $(n = 1, 2 \ldots)$. $\gamma_n = \sqrt{2V_0 - k_n^2}$, and R_n and T_n are reflection and transmission coefficients. Similarly, for the electronic motion in the surface plane $(x, y$-plane$)$, wave packets $\phi_l(x)$ and $\phi_m(y)$ are obtained by superimposing plane waves in small momentum intervals of lengths δ_x and δ_y, with centroid momenta k_l and k_m $(l, m = 1, 2 \ldots)$,

$$\phi_l(x) = \sqrt{\frac{\delta_x}{2\pi}} \frac{2\sin(\delta_x x/2)}{\delta_x x} e^{ik_l x} , \qquad \phi_m(y) = \sqrt{\frac{\delta_y}{2\pi}} \frac{2\sin(\delta_y y/2)}{\delta_y y} e^{ik_m y} . \qquad (8)$$

For sufficiently small δ_x, δ_y and δ_z, the "metal part" of the total wave function $\Psi(\vec{r}; t)$ in (2) can now be approximated by

$$\int d\vec{k} \, \rho(\vec{k}) \, b_{\vec{k}}(t) \, \phi_{\vec{k}}(\vec{r}) \, e^{-i\epsilon_{\vec{k}} t} \approx \sum_{\alpha} b_{\alpha}(t) \, \phi_{\alpha}(\vec{r}) \, e^{-i\epsilon_{\alpha} t} , \qquad (9)$$

where

$$\phi_{\alpha}(\vec{r}) = \phi_l(x) \, \phi_m(y) \, \phi_n(z) \quad \text{and} \quad \epsilon_{\alpha} = \frac{k_l^2}{2} + \frac{k_m^2}{2} + \frac{k_n^2}{2} - V_0 , \qquad (10)$$

with $\alpha = (l, m, n)$. The functions $\phi_{\alpha}(\vec{r})$ are orthogonal and normalized. Expanding the wave function $\Psi(\vec{r}; t)$ in these wave packets results in a set of coupled differential equations for the coefficients a_j and b_{α} that can be solved numerically for a given initial occupation [8],

$$i \begin{pmatrix} 1 & : & \langle \psi_j | \phi_{\alpha} \rangle \\ \dots\dots\dots & . & \dots\dots\dots \\ \langle \phi_{\alpha} | \psi_j \rangle & : & 1 \end{pmatrix} \begin{pmatrix} e^{-i\epsilon_j t} & : & 0 \\ \dots & . & \dots \\ 0 & : & e^{-i\epsilon_{\alpha} t} \end{pmatrix} \begin{pmatrix} \dot{a}_j(t) \\ . \\ \dot{b}_{\alpha}(t) \end{pmatrix}$$

$$= \begin{pmatrix} \langle \psi_j | V_f | \psi_{j'} \rangle & : & \langle \psi_j | V_i | \phi_{\alpha} \rangle \\ \dots\dots\dots\dots & . & \dots\dots\dots\dots \\ \langle \phi_{\alpha} | V_i | \psi_j \rangle & : & \langle \phi_{\alpha} | V_i | \phi_{\alpha'} \rangle \end{pmatrix} \begin{pmatrix} e^{-i\epsilon_j t} & : & 0 \\ \dots & . & \dots \\ 0 & : & e^{-i\epsilon_{\alpha} t} \end{pmatrix} \begin{pmatrix} a_j(t) \\ . \\ b_{\alpha}(t) \end{pmatrix} . \qquad (11)$$

For a translationally invariant surface and a perpendicularly incident projectile, we take advantage of the cylindrical symmetry and discretize the continuous distribution of metal electron momenta along the z and ρ axis. Fig. 4 shows results for hydrogen atoms, initially
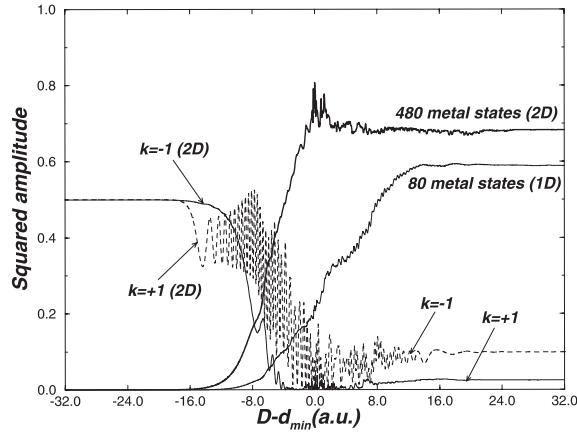
6

Fig. 4   Evolution of the squared amplitudes of the $|nkm\rangle = |2 \pm 10\rangle$ projectile state and all 480 included metal wave packets for incident $2p_0$–excited hydrogen atoms reflected off an aluminum surface. The metal occupation evolution is also shown for a separate calculation with 80 wave packets.

excited to the $2p_0$ state and perpendicularly incident with speed $v_z = 0.02$ on an Al surface. The time evolution of the system was calculated along a reflected classical trajectory of the projectile. The distance of closest approach to the jellium egde, $d_{\min} = 0.5$, was determined from a planar–averaged Thomas-Fermi-Molière potential [17] for the atom–surface interaction. A total of 480 wave packets ϕ_α (80 for the z and 6 for the ρ degrees of freedom) and hydrogen states with $n \leq 3$ and $m = 0$ are included. The occupation evolution of the atomic $2p_0$ level is given in parabolic representation, with electric quantum numbers k= ± 1. The metal occupation $\sum_\alpha |\phi_\alpha|^2$ is shown for the calculation with 480 metal states and for a separate calculation with 80 metal states for the z direction and only one wave packet, centered at $k_\rho = 0$, for the ρ direction. As expected, the metal population increases more rapidly for the calculation with 480 metal states, due to the inclusion of more substrate levels for the active electron's probability density to dissipate into.

The metal basis states (7) are localized in a volume of depth $\sim 1/\delta_z$ and, during the wave function evolution, electronic probability density is reflected at the "bulk" end of that volume. However, unphysical "recurrence effects" do not influence the atomic level occupation probabilities in the figure since the recurrence time exceeds the interaction time with the surface.

2.2. Numerical wave function propagation

Apart from contributing to the qualitative understanding of the interaction mechanisms, e.g., through computer animations, the direct propagation of the wave function on a numerical grid also enables the quantitative assessment of (one–electron) charge transfer. This method is flexible in that there are practically no restrictions to the effective one–electron potential used to describe the surface and projectile electronic structure (and the perturbations induced during the interaction). This allows for the detailed investigation

of the influence of crystal orientation, surface states, and image states of the substrate on the transfer of charge to and from a projectile [18].

Resonance positions and widths can be obtained by propagating the initial electronic state of the projectile Ψ_0 under the influence of the surface potential while keeping the ion at a *fixed* location $\vec{D}$ in front of the surface. The wave function at any time t is given by

$$\Psi(\vec{r}, \vec{D}, t) = \exp\{-iH(\vec{r}, \vec{D})\,t\}\ \Psi_0(\vec{r}, \vec{D})\,, \quad H = T + V_{surface} + V_{atom} \tag{12}$$

The ion–survival probability is obtained by following the reflected projectile until the integrated probability density around the projectile has reached a stable value.
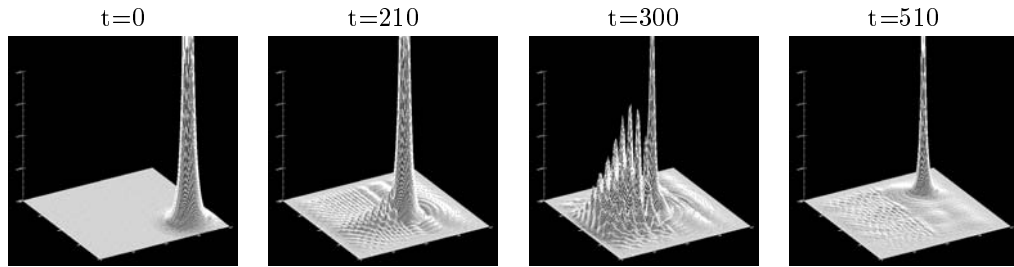
| t=0 | t=210 | t=300 | t=510 |

Fig. 5   Charge–transfer during the interaction of H^- ions with a model aluminum surface. The ion is incident from the lower right corner of the x–z plane and is reflected to the upper left corner. The plot shows $ln|\psi(x, 0, z, t)|^2$ obtained by three dimensional wave function propagation.

Fig. 5 shows the electronic probability density evolution for the scattering of H^- on a metal surface. The exploratory calculation is based on the corrugated surface potential

$$V_{surface}(\vec{r}) = 0.5[\Theta(z) - 1][1 + 0.5\cos(x)\cos(y)\cos(z)] \tag{13}$$

where $\Theta(z) = atan(z)/\pi + 0.5$ is a smeared–out step function. The effective potential for H^- was modeled by regularizing the potential

$$V_{atom}(r_p) = -(1 + \frac{1}{r_p})\exp(-2r_p) - \frac{\alpha}{r_p^4}\exp(-\frac{r_0^2}{r_p^2}) \tag{14}$$

at the origin. r_p measures the distance from the projectile center, $\alpha = 2.25$ is the atomic polarizability of H, and $r_0^2 = 2.547$. V_{atom} allows for the computation of the negative–ion ground state Ψ_0 of H^- and reproduces its affinity (0.75 eV). The propagator in (12) was constructed using the split–operator Crank–Nicholson technique on a 251 x 151 x 251 numerical grid with constant grid spacing, covering 100 x 60 x 100. a.u.^{3} in coordinate space. We used 151 grid points in the direction perpendicular to the scattering plane. The figure shows frames for the electron probability distribution in the scattering plane (at $y = 0$) at various times. The projectile was led along a broken–straight–line trajectory, starting at $t = 0$ at a distance of 30 a.u. from the jellium edge of the surface with an incident velocity $(v_x, v_z) = (0.1, -0.1)$ and with $d_{min} = 2$. Boundary conditions at the edge of the grid were imposed by a suitable absorptive complex potential. Shortly after $t = 510$ (last frame in Fig. 5), the resonant flux of electron probability density has stopped.

8

The ion–survival probability, obtained by integration over the atomic probability density at $t = 600$ amounts to 0.07.

3. Extended classical over–barrier simulations

3.1. Interactions at large ion–surface distances

The COM represents the transfer of electrons between valence states of a metal surface and energetically shifted hydrogenic projectile levels in terms of a continuous current of electronic charge [1,9,17,19]. This current sets in at large ion–surface distances D, when the potential barrier of the effective electronic potential $V_{\mathrm{eff}} = V_{\mathrm{proj}} + V_{\mathrm{im}}$ drops below the workfunction W of the target. The sequential capture of several electrons into excited states leads to the formation of a "hollow" projectile ion on the incident trajectory. For metal surfaces, V_{eff} includes the potential of the projectile core, V_{proj}, and classical image potentials V_{im} which represent the electronic response of the surface to the external charges of the projectile core and to the active electron. For insulating targets, the comparatively weaker dielectric response has been accounted for in terms of modified image potentials that involve approximate dielectric functions [17,20].

The original COM [9] combines estimated rates for resonant over–barrier capture, Γ_n^{RC}, resonant loss, Γ_n^{RL}, Auger transitions that fill a particular projectile shell n, $\Gamma_{n',n}^{\mathrm{A-Gain}}$, and Auger transitions that deplete shell n, $\Gamma_{n',n}^{\mathrm{A-Loss}}$, in a system of rate equations for the dynamically changing populations a_n of projectile shells with principal quantum numbers n. For both metal and insulating surfaces, the COM reproduces well measured kinetic energy gains on the incoming projectile trajectory, for a large range of projectile charges. The kinetic energy gain is the result of the acceleration toward the surface of a charged projectile due to the interaction with its image charge. Measurements of kinetic energy gains are primarily sensitive to distant interactions with the surface, and an incident ion has accumulated over 70 % of its net energy gain by the time it reaches the critical distance D_1^* for the first over–the–barrier capture of a surface electron.
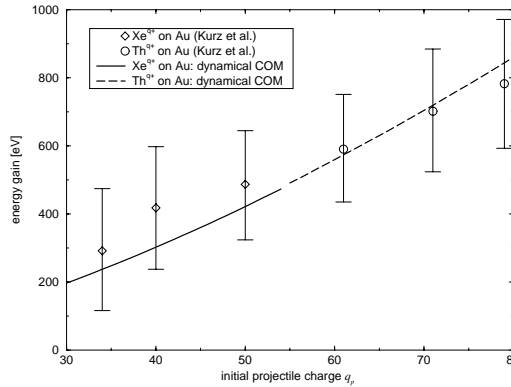

Fig. 6   Experimental [10] and simulated [19] kinetic energy gains for highly charged ions on gold surfaces.

As an example, Fig. 6 shows measured [10] kinetic energy gains for a large range of inci-

dent projectile charges q_p in comparison with results from extended COM simulations [19]. The figure complies with the $q_p^{3/2}$ – proportionality of the kinetic energy gain, obtained by assuming that the projectile is instantaneously and completely neutralized at D_1^*. It thus confirms the primary dependence of the projectile kinetic energy gain on D_1^*.

3.2. Interactions at small ion–surface distances

As the HCI moves closer to the topmost surface layer, electrons that were previously captured into highly excited states get increasingly disturbed and eventually lost. For incident ion energies of up to several 100 keV and for a wide range of initial ion charge states and target materials, experiments on the final charge distribution of reflected projectiles have shown that the vast majority of the projectiles emerges in a neutral charge state [21,22]. It also became clear, that a "side feeding (SF)" mechanism leads to complete neutralization even in cases where the energies of projectile and target inner shells do not match and where, in consequence, an interpretation in terms of the resonant transfer of independent electrons fails. This stimulated the investigation of rapid inner–shell transfer mechanisms (referred to as SF) that involve more than one active electron.

Recent extensions to the original COM include these electron transfer and emission processes at small distances D where strong overlap between target and projectile orbitals occurs. While no detailed quantum dynamical calculations are available, carefully modeled SF rates Γ_n^{SF} can account for the rapid filling of inner projectile shells observed in emitted Auger electron spectra and final charge-state distributions of grazingly reflected projectiles (cf. refs. [19] and references therein).

Other prominent near–surface interaction mechanisms are the loss of loosely bound projectile electrons due to additional screening enforced by the tightly packed induced charge cloud (so–called "peeling off (PO)") [9] and electron loss due to the promotion of occupied inner projectile levels into resonance with empty conduction band states ("continuum promotion (CP)"). In modeling PO rates, we included dynamic effects by assuming that a captured electron may be peeled off only after a certain time delay which is related to the electron's orbital period. We also included screening effects by disabling PO for orbital radii $< r_n >$ smaller than the surface screening length [19].

The time–dependent projectile occupations a_n can be obtained as solutions to the set of rate equations [17,19],

$$
\begin{aligned}
\frac{da_n}{dt} &= \theta(A_n - a_n)\Gamma_n^{RC} - a_n\Gamma_n^{RL} + \sum_{n'>n}\Gamma_{n',n}^{AI} - 2\sum_{n'<n}\Gamma_{n,n'}^{AI} \\
&+ \theta(A_n - a_n)\Gamma_n^{SF} - a_n\Gamma_n^{PO} + \Gamma_n^{CP} \\
&- \delta_{n,M}\Gamma^{CK} - \delta_{n,L}\Gamma^{sCK} + (\delta_{n,K} - \delta_{n,L} - \delta_{n,M})\,a_L a_M \Gamma^{KLM}\,. \quad (15)
\end{aligned}
$$

The rates $\Gamma_n^{RC,RL}$ and $\Gamma_{n,n'}^{AI}$ are modeled according to the original COM. All other rates in (15) correspond to processes that occur at small ion–surface distances.

For hyper–thermal N^{6+} projectiles, we have modeled SF in analogy with recently calculated LCV Auger rates for the motion of an ion *inside* solid matter. LCV processes involve the transition of an electron out of the charge cloud (C), that dynamically follows

10

the projectile as it moves through the substrate electron gas, into a vacancy in the L shell while exciting plasmons and electron–hole pairs in the valence band (V). We adopted the interpretation of [23], but find best agreement of our simulation results for Al surfaces with measured projectile–final–charge states and emitted–electron spectra, for SF rates that exceed the ones given in [23] by about an order of magnitude [19].

In general, projectile sub–shells are not resolved. For the L-shell and applications to hyper–thermal N^{6+} projectiles, however, we kept track of the sub–shell populations [19]. We calculated projectile binding energies at the Hartree–Fock level. For any given projectile configuration vector $\{a_n\}$ occurring during the ion–surface interaction, we employed an atomic structure code to generate average configuration binding energies for all (undistorted) projectile shells, $\{\varepsilon_n^\infty(\{a_n\})\}$. We assumed that the $2p$ level is preferentially populated via Auger ionization (AI) and SF processes, as suggested by its higher degeneracy. With increasing occupation of the L-shell, relaxation via LLM Coster–Kronig (CK) and LLL super CK (sCK) transitions becomes energetically possible and proceeds by one and two orders of magnitude faster, respectively, than other Auger processes. The rates for CK, sCK, and KLM Auger transitions are included in the last line of (15)

For the integration of (15), together with Newton's equation for the projectile trajectory $\vec{D}(t)$, we used a Monte–Carlo method with an ensemble of 5000 incident particles [19]. The classical motion of the projectile is determined by the self–image force of the projectile ion and binary Thomas–Fermi–Moliére forces between the projectile and individual surface atoms, including recoil effects. Starting at a projectile position above the critical distance D_1^*, the HCI is propagated with finite time steps Δt_i from one point in time, t_i, to the next, t_{i+1}, along its trajectory. At each time t_i, separate values Δt_i for each transition type (AI,RC,RL,SF,PO, etc.), are drawn from an exponential random number distribution with a mean value equal to the transition time, i.e., to the inverse of the respective transition rate Γ. The physical process supplying the smallest Δt_i is chosen to take place, all variable parameters, such as configuration energies, are updated according to the change in $\{a_n(t)\}$, and the projectile is moved from $\vec{D}(t_i)$ to $\vec{D}(t_{i+1})$.

3.3. Electron emission spectra and yields

Apart from AI setting in as soon as more than two electrons have been captured, SF, PO, and CP contribute to the total electron yield. Fig. 7a shows low-energy electron spectra for N^{6+} interacting with an Al(111) surface under $\Theta = 45°$ for asymptotic incident energies $E_{kin} = 10$ eV and 80 eV. For this system, the image energy gain amounts to about $E_{gain} = 14$ eV. The spectra in Fig. 7a are normalized to the total incident particle current. The experimental data have been corrected for the spectrometer transmission and are scaled up from emission into the acceptance solid angle of the spectrometer (0.031 sr) to emission into a full 4π sphere. The simulated data have been convoluted with the spectrometer resolution of 0.7%. Integrating the spectral yields above 20 eV leads to yields of 5.7 and 5.8 emitted electrons per incident ion for the simulated spectra and to 4.9 and 4.3 for the experiments with $E_{kin} = 10$ eV and 80 eV, respectively. Fig. 7b shows projectile K–Auger spectra for N^{6+} colliding with an Al(111) surface. The peak widths are related to the range of different initial L–sub–shell populations at the time of K–Auger

decay. In general, the KLL sub–peak intensities sensitively depend on the ratio between the L–shell filling rate and KLL decay rates which are only known for free ions.
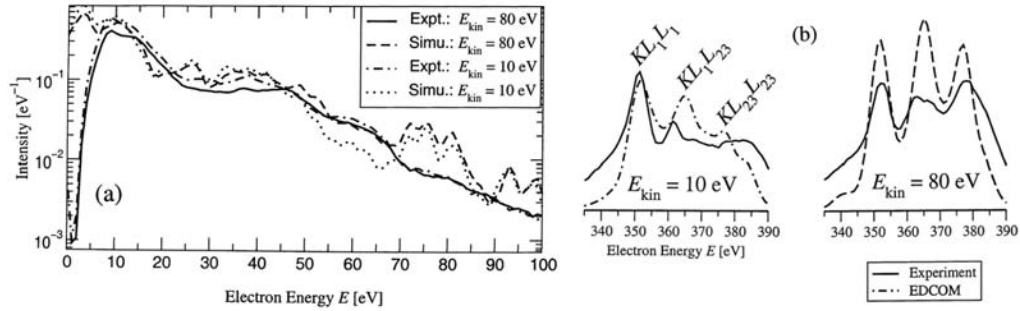

Fig. 7 Experimental and simulated (EDCOM) electron–emission spectra for 10 eV and 80 eV N^{6+} projectiles and an Al(111) surface [19]. (a) Low-energy spectra. (b) KLL spectra.

For increasing E_{kin}, the KL_1L_1 peak loses intensity which is transferred into the upper part of the KLL spectrum. This can be understood in view of the vertex of the trajectory moving closer to the topmost surface layer at higher E_{kin} [15], resulting in stronger SF at the time of K–Auger emission. The upper edge of the experimental $KL_{23}L_{23}$ peak appears at a higher energy than in the simulation. In order to simulate the higher KLL energy, all six neutralizing electrons had to be present in the L–shell. For $E_{kin} = 80$ eV, we find an average L–shell occupation of 4.6 at the time of the K–Auger decay.

3.4. Final charge–state distributions

We simulated [19] fractions of the final projectile charge states $0 \leq q_{\text{final}} \leq 2$ for ground state (gs) H-like ions and meta–stable (mt) He-like second row ions in (1s2s) configurations colliding at $E_{kin} < 100$ eV and a grazing angle of $\Theta = 5°$ with Al(111). The simulated charge–state distributions are strongly dominated by neutral reflected projectiles, in agreement with typical experimental results (at higher incident kinetic energies [21]).

For hyper–thermal hydrogenic and (1s,2s)–meta–stable carbon, nitrogen, and oxygen projectile ions, our [19] charge–state distributions vary slightly with the projectile nuclear charge and are rather insensitive to the number of initial K–vacancies.

4. Summary and outlook

The self–energy method allows for the efficient computation of level shifts and widths. We used this method for the generation of surface resonances (for nuclear charges up to $Z = 4$ near a metal surface) that serve as basis functions for the solution of the time-dependent Schrödinger equation. Results for ion yields in collisions of H with an Al-surface show that quantum mechanical dynamic couplings play a minor role at sub–thermal velocities but lead to a significant rearrangement of the charge density for perpendicular velocities greater than 10^{-3} a.u. For highly charged projectiles, we have included atomic structure calculations, Monte–Carlo sampling along the entire reflected projectile trajectory, and

12

simulated electronic processes near the surface within an extended COM. Our simulation results comply with measured projectile kinetic energy gains, electron emission yields, and final charge–state distributions. This agreement has been achieved *without* adapting the simulation to a particular collision system or measured quantity.

Recently, the interaction of atoms and ions with thin metallic films has attracted attention [24,25]. One expects novel phenomena to occur in this type of interaction due to the confinement of the electronic motion in the growth direction of the film and to the associated quantization of the energy spectrum ("size quantization"), in much the same way as in semiconductor quantum-well structures. Size quantization in the growth direction of the film gives rise to characteristic structures in level widths, atomic occupation probabilities, and transition distances as a function of the film thickness. The large variation of the calculated transition distances with the film thickness may result in observable effects in atomic interactions with thin films [25].

Acknowledgments

References

1. J. Burgdörfer, in: Review of Fundamental Processes and Applications of Atoms and Ions, ed. C.D. Lin (World Scientific, Singapore, 1993) p. 517.
2. F. Martín and M.F. Politis, Surf. Sci. **356**, 247 (1996).
3. P. Nordlander, Phys. Rev. B **53**, 4125 (1996).
4. A.G. Borisov, R. Zimny, D. Teillet-Billy, and J.P. Gauyacq, Phys. Rev. A **53**, 2457 (1996).
5. S.A. Deutscher, X. Yang, and J. Burgdörfer, Phys. Rev. A **55**, 466 (1997).
6. P. Kürpick, U. Thumm, and U. Wille, Phys. Rev. A **56**, 543 (1997).
7. P. Kürpick, U. Thumm, and U. Wille, Phys. Rev. A **57**, 1920 (1998).
8. B. Bahrim, P. Kürpick, U. Thumm, and U. Wille, Nucl.Instr.Meth. B **164**, 614 (2000).
9. J. Burgdörfer, P. Lerner, and F.W. Meyer, Phys. Rev. A **44**, 5674 (1991).
10. H. Kurz *et al.*, Phys. Rev. A **49**, 4693 (1994).
11. J. Limburg *et al.*, Phys. Rev. A. **51**, 3873 (1995).
12. J.P. Briand *et al.*, Phys. Rev. A **53**, R2925 (1996).
13. Q. Yan, D.M. Zehner, and F.W. Meyer, Phys. Rev. A **54**, 641 (1996).
14. A. Arnau *et. al*, Surf. Sci. Rep. **27**, 113 (1997).
15. J. Thomaschewski *et al.*, Phys. Rev. A**57**, 3665 (1998).
16. S. B. Hill, C. B. Haich, Z. Zhou, and P. Nordlander, Phys. Rev. Lett. **85**, 5444 (2000).
17. J.J. Ducrée, F. Casali, and U. Thumm, Phys. Rev. A**57**, 338 (1998).
18. A.G. Borisov, A.K. Kazansky, and J.P. Gauyacq, Phys. Rev. Lett. **80**, 1996 (1998).
19. J.J. Ducrée, H.J. Andrä, and U. Thumm, Phys. Rev. A**60**, 3029 (1999).
20. L. Hägg, C.O. Reinhold, and J. Burgdörfer, Phys. Rev. A**55**, 2097 (1997).
21. L. Folkerts *et al.*, Phys. Rev. Lett. **74**, 2204 (1995); Phys. Rev. Lett. **75**, 983 (1995).
22. S. Winecki, M. P. Stöckli, and C. L. Cocke, Phys. Rev. A **56**, 538 (1997).
23. R. Díez Muiño *et al.*, Phys. Rev. A **57**, 1126 (1998); Phys. Rev. Lett. **76**, 4636 (1996).
24. A. G. Borisov and H. Winter, Z. Phys. D **37**, 263 (1996).
25. U. Thumm, P. Kürpick, and U. Wille, Phys. Rev. B **61**, 3067 (2000).